atmosphere

MDPI

Article

Causes of the Interannual Variation of Summer Precipitation in Eastern Southwest China

Chuhan Lu [1,2,*], Dingan Huang [3], Bo Chen [4] and Yingying Bai [5]

[1] Key Laboratory of Ecosystem Carbon Source and Sink, China Meteorological Administration (ECSS-CMA), Wuxi University, Wuxi 214063, China
[2] Key Laboratory of Meteorological Disaster of Ministry of Education, Nanjing University of Information Science & Technology, Nanjing 210044, China
[3] Sanming Meteorological Bureau, Sanming 365000, China; hda0125@163.com
[4] East China Air Traffic Management Bureau, CAAC, Shanghai 200335, China; eamc2022@atmb.cn
[5] CMA Key Open Laboratory of Transforming Climate Resources to Economy, Chongqing Climate Center, Chongqing 401147, China; byying113@126.com
* Correspondence: luchuhan@nuist.edu.cn

Abstract: Using ERA5 reanalysis data, we conducted an EOF analysis of summer precipitation in the eastern part of southwestern China (ESWC) over the past 60 years. Our study aimed to investigate the spatial distribution characteristics and interannual variability of summer precipitation in the ESWC, as well as to reveal the possible physical mechanisms influencing its interannual variability. The results indicate that, at the interannual scale, the first two modes of summer precipitation in the ESWC exhibit a uniform pattern and a north–south dipole pattern, respectively. The maximum and minimum time coefficients of the first mode correspond to the severe flood and drought events in 1998 and 2006, respectively, indicating that their time coefficients reflect the typical events well. The tri-pole sea surface temperature anomaly in the North Atlantic, along with the sea ice anomaly near the Barents Sea, induces a quasi-zonal wave train in the upper troposphere. This wave train propagates from the tropical and mid-latitude Atlantic, traverses the mid-high latitudes of Eurasia, and reaches the eastern part of China. The wave train induces cyclonic (anticyclonic) anomalies in the north (south) of the ESWC, facilitating the convergence of high-latitude dry and cold air with warm and moist southwesterly winds from the tropical ocean. This convergence promotes increased summer precipitation in the ESWC. We provided valuable insights into the interannual variability of summer precipitation in the ESWC, shedding light on the physical mechanisms responsible for these variations.

Keywords: eastern southwest China; interannual; causes of precipitation change; sea surface temperature anomaly

Citation: Lu, C.; Huang, D.; Chen, B.; Bai, Y. Causes of the Interannual Variation of Summer Precipitation in Eastern Southwest China. *Atmosphere* **2023**, *14*, 1230. https://doi.org/10.3390/atmos14081230

Academic Editor: Abd Al Karim Haj Ismail

Received: 14 June 2023
Revised: 6 July 2023
Accepted: 12 July 2023
Published: 31 July 2023

1. Introduction

Weather and climate play a crucial role in human life, and precipitation as a key component of weather and climate change has garnered significant attention from meteorologists. The Yangtze River Basin (YRB) is known for its abundant precipitation. Numerous scholars have examined the spatiotemporal variations of precipitation in the YRB, yielding substantial achievements. Research findings indicate an increasing trend in summer precipitation and extreme precipitation events in the YRB [1–3], with notable disparities in the spatial distribution of extreme precipitation [4].

The ESWC, spanning from 27° to 32° N and 105° to 110° E, is situated in the upper reaches of the YRB. The interannual variation characteristics of summer precipitation in this region differ from those observed in the middle and lower reaches of the YRB. The ESWC experiences significant interannual variation in summer precipitation, often accompanied by frequent droughts and floods [5]. For instance, in 2020, June and July

witnessed the highest precipitation levels in the ESWC since 1961, with frequent heavy rain events covering a wide area [6]. Conversely, the prolonged drought in 2022 led to severe wildfires in Chongqing, exerting a significant impact on society and people's lives. Consequently, understanding the causes of droughts and floods has become a subject of great interest [7,8].

The interannual variation of precipitation is influenced by multiple factors. Southwest China is affected by both the East Asian monsoon and the South Asian monsoon, although their impacts on regional precipitation differ. Previous studies have indicated that the East Asian monsoon has a greater influence on the eastern part of Chongqing compared to the western part, while the western part is primarily affected by the South Asian monsoon. There is a clear negative correlation between Chongqing's precipitation and the intensity of the East Asian monsoon. Specifically, the summer precipitation in Chongqing decreases with the increasing intensity of the East Asian monsoon [9]. Ma et al. [10] observed a significant influence of the East Asian monsoon on precipitation in southwest China. During severe droughts in the Sichuan Basin in summer, the East Asian monsoon weakens considerably, and the East Asian monsoon trough and rain belt shift southward. Although the East Asian monsoon and the South Asian monsoon are relatively independent systems [11], their synergy also has a significant impact on summer precipitation in southwest China [12]. Additionally, the position change of the summer subtropical high is closely related to the summer precipitation anomaly in the ESWC [5].

Precipitation in southwest China is also influenced by various external forcing factors, such as surface thermal effects [13,14], Tibetan Plateau vegetation [15,16], snow cover [9,17], intra-seasonal oscillations of the tropical atmosphere [18], and sea surface temperature (SST) anomalies. The correlation between SST anomalies and summer precipitation in southwest China has attracted significant attention from meteorologists. Numerous studies have demonstrated that events like the El Niño Southern Oscillation (ENSO), the Western Pacific warm pool, Indian Ocean SST anomalies, and South China Sea SST anomalies can influence large-scale circulation systems such as the Asian monsoon, the Western Pacific subtropical high, and the South Asia high, consequently affecting China's weather and climate [19–25]. For instance, Li et al. [22] highlighted that elevated SST in the equatorial Middle East Pacific and the Indian Ocean during spring enhances the intensity and southward shift of the South Asia high and the Western Pacific subtropical high during summer, leading to increased areal coverage of these high-pressure systems. Consequently, the intensity of the East Asian summer monsoon and South Asian summer monsoon weakens, and upward vertical motion is observed in the ESWC, promoting precipitation formation. Pang et al. [26] discovered that the SST anomaly in the equatorial Middle East Pacific can modulate the activity of the Western Pacific subtropical high, ultimately influencing summer precipitation in the southwest region.

The ESWC is situated in close proximity to the Qinghai–Tibet Plateau and Sichuan Basin in the west, the Yunnan–Guizhou Plateau and Qinling Plateau in the north and south, resulting in a unique topography and significant land–sea–air interactions. It experiences a subtropical monsoon climate and is located at the convergence of different climatic zones, making it prone to frequent summer droughts and floods [27]. Understanding the causes of summer precipitation changes in the ESWC holds great practical significance. Therefore, this study utilizes ERA5 reanalysis data to analyze the interannual variation characteristics of summer precipitation in the ESWC over the past 60 years and investigates the potential factors influencing its interannual variability. The findings aim to provide a theoretical foundation for improving summer drought and flood prediction techniques in the ESWC.

2. Data and Methods

2.1. Data

The data used in this paper mainly include monthly ERA5 reanalysis data from 1961 to 2020 [28]. Major physical quantities include precipitation, sea temperature, sea ice concentration, geopotential height, temperature, zonal wind, meridional wind, vertical

velocity, and vertical integral of one-way (north and east) water vapor flux. The horizontal resolution is 0.25° × 0.25°, and in the vertical direction is divided into 37 layers.

2.2. Methods

In this paper, two-dimensional wave activity flux [29] is used to analyze the relationship between Atlantic SST anomalies and the inter-annual variation of summer precipitation in ESWC. The specific formula is as follows:

$$W = \frac{1}{2|\overline{U}|}\begin{bmatrix} \overline{u}(\psi_x'^2 - \psi'\psi'_{xx}) + \overline{v}(\psi'_x\psi'_y - \psi'\psi'_{xy}) \\ \overline{u}(\psi'_x\psi'_y - \psi'\psi'_{xy}) + \overline{v}(\psi_y'^2 - \psi'\psi'_{yy}) \end{bmatrix} \quad (1)$$

where ψ' represents the perturbed flow function, $\overline{u}$ and $\overline{v}$ are the basic flow, respectively, and the subscript represents the partial derivative of the perturbed flow function with respect to the x and y directions, respectively. The direction of the two-dimensional wave flux is consistent with the direction of the Rossby wave group velocity, that is, the direction of wave energy propagation.

3. Results

3.1. Interannual Variation Characteristics of Summer Precipitation

In order to examine the spatial distribution and interannual variation characteristics of summer precipitation in the ESWC, an EOF decomposition of summer precipitation spanning the past 60 years was conducted. As depicted in Figure 1, the first mode of precipitation exhibits a variance contribution of 52.90%, while the second mode contributes 17.96%. These larger variance contributions indicate a significant convergence of summer precipitation in the ESWC. The first mode represents a uniform pattern, reflecting the most representative spatial distribution pattern of summer precipitation. The area with large precipitation values is predominantly located in the central and eastern parts of the region, particularly in the southeastern area of Chongqing, suggesting that this region is highly susceptible to variations in summer precipitation. On the other hand, the second mode displays a north–south dipole pattern, with positive values in the southeast and negative values in the northwest. More specifically, when there is increased precipitation in the southeast, there tends to be reduced precipitation in the northwest, and vice versa.

The direction of the corresponding feature vector can be determined from the positive and negative values of the time coefficient of the feature vector (Figure 1b,d). The magnitude of the time coefficient indicates the degree of typicality of the spatial distribution pattern of summer precipitation in the ESWC for a given year. Analyzing the time coefficient of the first mode (PC1) of summer precipitation in the ESWC reveals that out of the 60-year period from 1961 to 2020, 27 years exhibit positive time coefficients while the remaining 33 years have negative time coefficients. PC1 effectively captures the precipitation characteristics of representative years, where positive index years correspond to higher overall summer precipitation in the ESWC, and vice versa. Notably, the region experienced historically rare extreme climatic events in the summer of 1998 and 2006, characterized by flood and drought, respectively, which align with the maximum and minimum values of PC1. Additionally, the recent heavy precipitation year (2020) also corresponds to relatively large PC1.

By examining the time coefficient of the second precipitation mode (PC2), it can be seen that positive PC2 years primarily indicate increased summer precipitation in the southeast and reduced precipitation in the northwest of the ESWC. Precipitation gradually decreases from the southeast to the northwest. Conversely, negative PC2 years show an increasing precipitation gradient from the southeast to the northwest. The years 1961 and 1969 correspond to the maximum and minimum values of PC2, respectively.

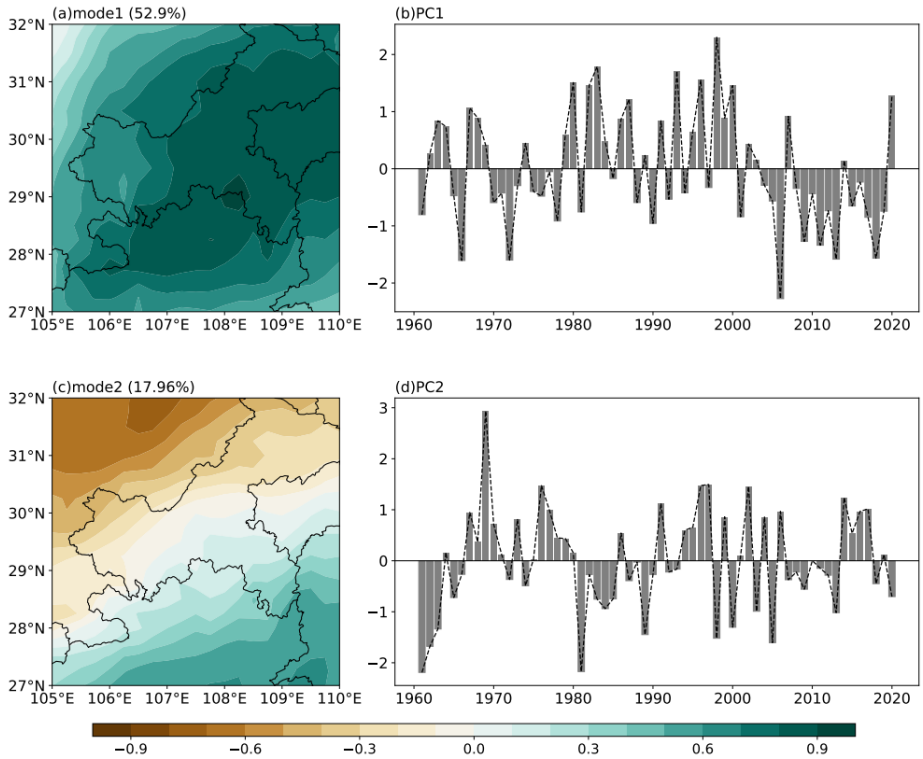

Figure 1. The spatial distribution patterns and time coefficients of the first mode (**a**,**b**) and the second mode (**c**,**d**) of summer precipitation in the ESWC.

To further show the reliability of the aforementioned analysis, we present the difference values between the maximum and minimum time coefficients of the first two modes in the EOF analysis of summer precipitation in the ESWC (Figure 2). It is evident that the difference in precipitation distribution is consistent with the patterns observed in the two modes (Figure 1), namely, the region-wide consistent type and the north–south reverse type. In the first mode, the area exhibiting large differences in precipitation distribution during typical years (Figure 2a) is located in the central and eastern parts of the region, with a maximum difference of 713.10 mm. Conversely, in the second mode, the difference in precipitation distribution during typical years (Figure 2b) gradually decreases from the southeast to the northwest of the region, with a maximum difference of 950.37 mm.

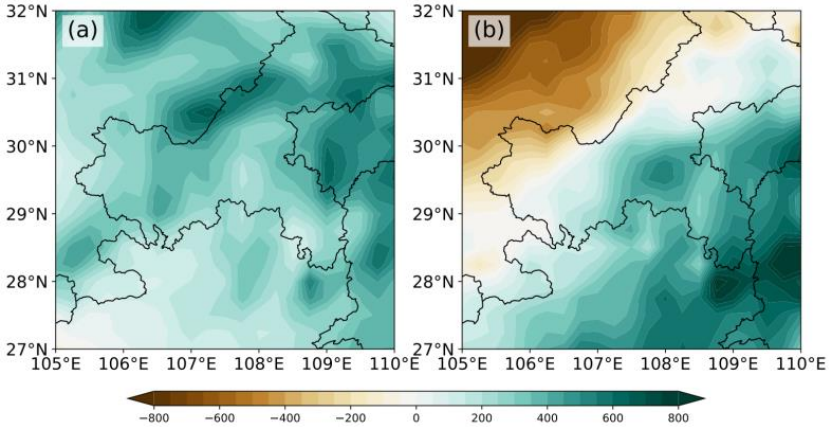

Figure 2. The difference of summer precipitation distribution in typical years in the ESWC (unit: mm): (**a**) 1998 and 2006; (**b**) 1969 and 1961.

3.2. Causes of Interannual Variation in Summer Precipitation

Previous studies have demonstrated that the inherent mechanism of changes in two-dimensional elements can be simplified to analyze the time coefficient of its modes [30–32]. In Section 3.1, we compare and analyze the spatial distribution patterns and time coefficients of the first and second modes of summer precipitation in the ESWC. The first mode of precipitation exhibits a variance contribution of 52.90%, indicating its dominant role in the summer precipitation model in the ESWC. Building upon the findings presented in Section 3.1, this section utilizes PC1 to investigate the circulation anomaly configuration associated with the increase (decrease) in summer precipitation in the ESWC.

3.2.1. Water Vapor Conditions and Vertical Motion

The factors directly influencing precipitation in the region are the water vapor condition and vertical motion. Therefore, Figure 3 illustrates the regression coefficient of PC1 on the water vapor flux throughout the entire layer, and the vertical velocity at 850 hPa to represent vertical motion in the lower troposphere. From the perspective of water vapor transport conditions, the ESWC is situated at the convergence area of cold air from the northwest and warm and humid air from the southwest to the ESWC, resulting in noticeable horizontal shear in the wind direction of water vapor transport. The southern (northern) region to the ESWC exhibits an anticyclonic (cyclonic) anomaly of water vapor (Figure 3a). Specifically, the anticyclone in the northwest Pacific on the northwest side exhibits a significant southwest water vapor transport anomaly, conveying warm and humid air from the tropical ocean to the ESWC, where it intersects with the northwest cold air from the mid-latitudes. In addition, there is a small local cyclonic circulation in the ESWC which may induce enhanced ascent and greater rainfall. According to the w equation, warm advection in the lower layer facilitates vertical upward motion and the generation of precipitation [33]. In terms of vertical velocity at lower levels, most parts of the ESWC region experience prevailing ascending motion (Figure 3b), while the western Pacific experiences prevailing sinking motion, both of which contribute to increased precipitation.

3.2.2. Circulation Configuration and Wave Activity Flux

According to the analysis in Section 3.2.1, the anticyclonic–cyclonic dipole water vapor transport anomaly on the north and south sides of the ESWC contributes to the formation of precipitation in the region. To further investigate the atmospheric circulation anomalies responsible for the water vapor transport configuration and their impact, Figure 4 presents the regression coefficients of PC1 on the atmospheric fields. It can be observed that the upstream region of the ESWC exhibits the pronounced alternation of positive and negative wave-like circulation from the northwest Atlantic Ocean to the western Pacific Ocean. And as PC1 increases, a deep, westward-inclined anticyclonic anomaly emerges in the northwest Pacific region east of south China, accompanied by a southwest airflow on its northwest side, corresponding to the strong southwest warm and humid water vapor transport shown in Figure 3a. Simultaneously, in the middle and upper troposphere, a distinct cyclonic circulation forms on the northern side of southwest China, while the northwest airflow on the southwest side leads to the convergence of mid-latitude cold air in the ESWC and the development of warm and moist cyclones on the southern side of southwest China. This suggests that the quasi-zonal wave train from the upstream region may serve as an important driving factor for the summer precipitation anomaly in the ESWC.

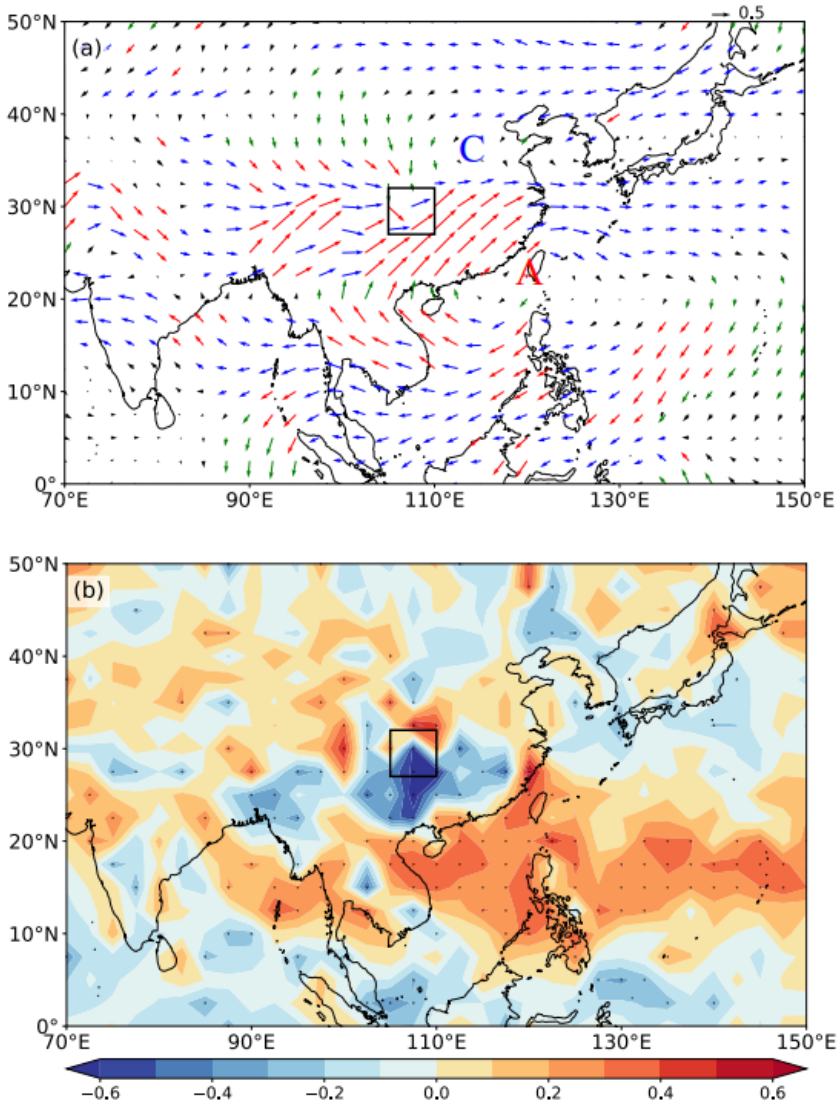

Figure 3. Regression coefficients of PC1 on (**a**) the vertical integration of water vapor flux in the whole layer (vector) and (**b**) 850 hPa wind field (shadow). Dotted areas in the figure indicate that the regression coefficients pass the 90% reliability test. The red, blue, and green arrows in the wind vector diagram represent the uv direction, u direction, and v direction, respectively, which pass the 90% reliability test. The black box indicates the location of the ESWC.

To provide a clearer description of the mid-latitude wave train circulation anomalies associated with summer precipitation over the ESWC, Figure 5 presents the vertical profile of the potential height composite difference along the wave train. It can be observed that the geopotential height anomaly generally aligns with the aforementioned characteristics of the upper quasi-zonal wave train. In particular, there is a pronounced "+ − +" type altitude anomaly oscillation in the southern regions of Iceland, the Norwegian Sea, the Barents Sea, and the west Siberian region, with relatively deep geopotential altitude anomalies. The largest anomaly values are observed in the upper troposphere, gradually decreasing towards the lower levels, indicating a downward propagation trend for the geopotential altitude anomaly signal.

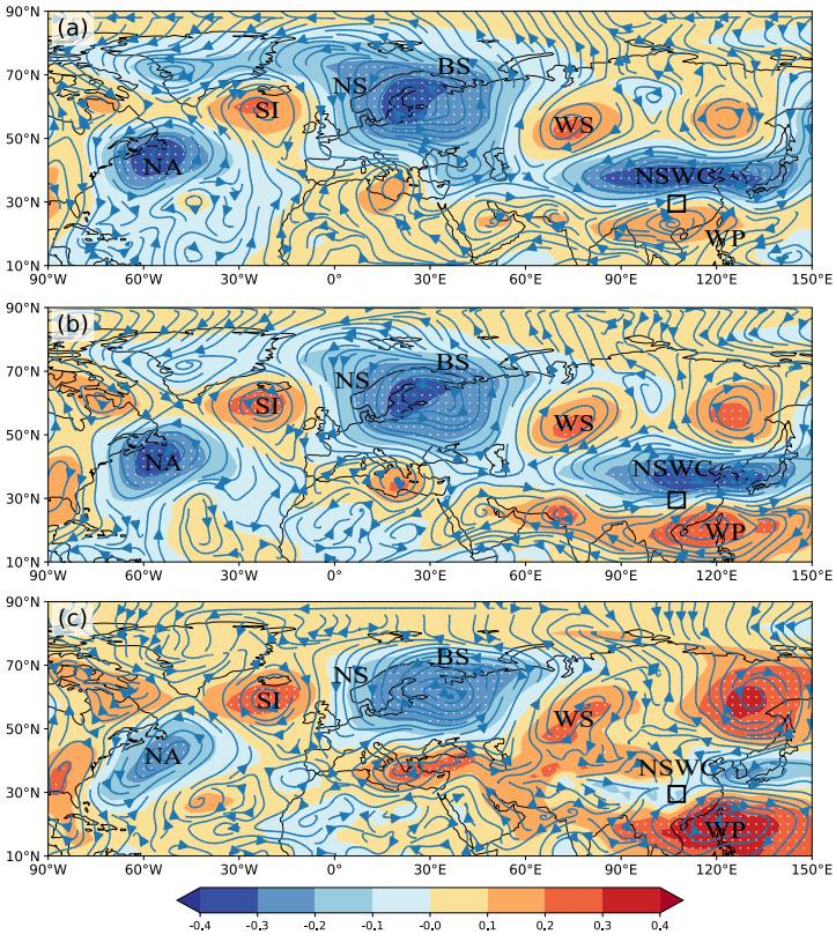

Figure 4. Regression coefficients of PC1, height field (shadow), and UV wind field (streamline) at three levels (**a**) 300 hPa, (**b**) 500 hPa, and (**c**) 850 hPa. Dotted areas in the figure indicate that the regression coefficients pass the 90% reliability test. NA, SI, NS, BS, WS, NSWC, and WP in the figure represent the North Atlantic, the southern regions of Iceland, the Norwegian Sea, the Barents Sea, western Siberia, the northern side of southwest China and the western Pacific, respectively.

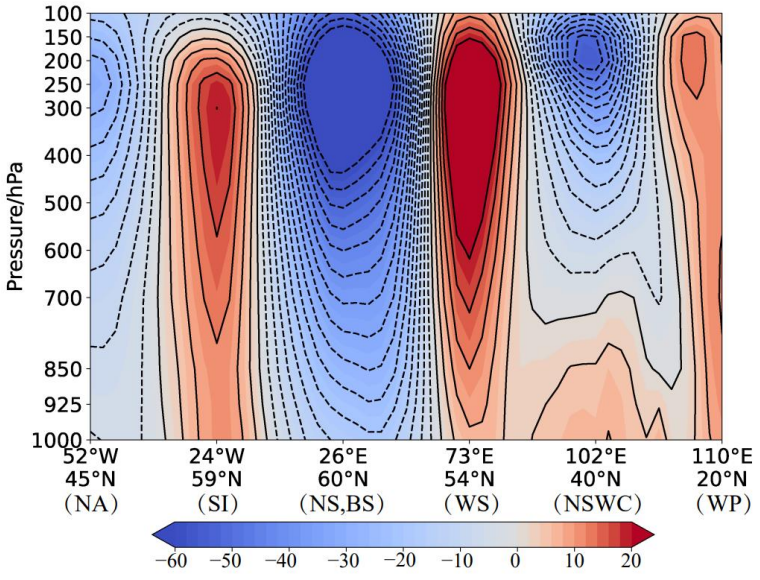

Figure 5. Vertical profile of the geopotential height composite difference along the propagation path of the wave activity flux (unit: gpm).

As depicted in Figures 4 and 5, a clear relationship emerges between anomalous summer precipitation in the ESWC and mid-latitude Rossby wave activity. To further elucidate the associated Rossby wave activity and the concurrent propagation of wave energy, Figure 6 illustrates the composite difference of the 300 hPa wave activity flux and the quasi-geostrophic stream function between high and low PC1 years. It is evident that, during years characterized by substantial positive anomalies of summer precipitation in the ESWC, notable eastward-propagating and dissipating Rossby wave activity features manifest in the mid to high latitudes of the Eurasian continent. This wave train efficiently transfers wave energy to the ESWC region through the Norwegian Sea and western Europe. This atmospheric teleconnection pattern bears a striking resemblance to the Eurasian–Pacific (EUP) pattern [34].

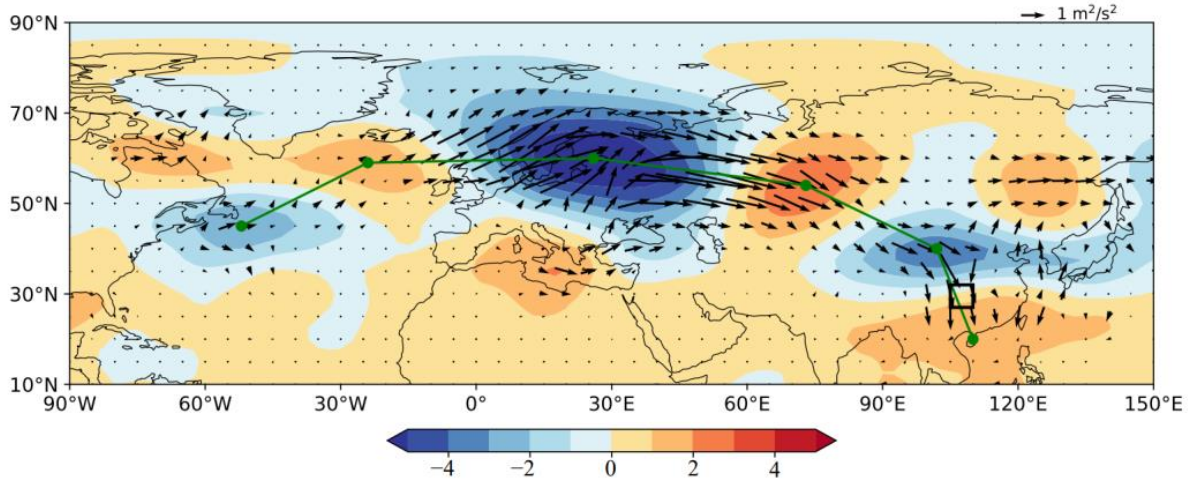

Figure 6. The composite difference of the 300 hPa wave activity flux (vector, unit: m^2/s^2) and the quasi-geostrophic stream function anomaly (shaded, unit: 10^6 m^2/s) between high and low PC1 years. The green solid line denotes the propagation path of the wave activity flux.

In general, Rossby waves are excited by various wave sources, with atmospheric divergence playing a substantial role in linear systems [35]. To provide a more precise depiction of the wave sources' variability, this study uses the source of Rossby wave activity (SRWS) term based on the potential vorticity equation [36]. The formula is as follows:

$$SRWS = -f\nabla \cdot V \quad (2)$$

where f represents the Coriolis force parameter and $\nabla \cdot V$ denotes wind divergence.

The composite difference of SRWS in Figure 7 reveals that the significant locations of wave sources and sinks align closely with the propagation path of the wave activity flux. Positive RWS anomalies of significance are observed in the tropical Atlantic Ocean, as well as in the vicinity of the Greenland Sea and the Norwegian Sea. These anomalies contribute to the excitation of high-level atmospheric Rossby waves [37]. The formation and propagation of Rossby waves play a crucial role in modulating the development of anomalous wave-train-like circulations, thereby exerting significant influence on summer precipitation in the ESWC.

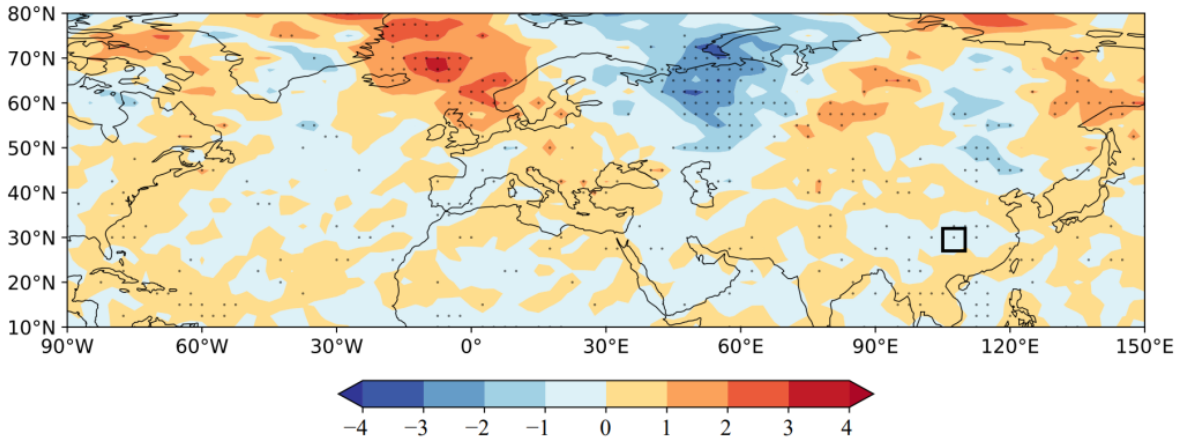

Figure 7. The 300 hPa SRWS (unit: 10^{-10} s^{-2}) composite difference between high and low PC1 years, with dotted areas indicating that they pass the 90% reliability test.

3.2.3. External Forcing Factors

Anomalies in SST and sea ice coverage can induce local atmospheric circulation changes through non-adiabatic heating, subsequently affecting downstream areas through the dispersion of energy by Rossby waves [38–40]. To further analyze the driving factors behind the formation of the aforementioned wave train, the correlation coefficient between the PC1 for summer precipitation in the ESWC and concurrent SST was calculated (Figure 8). It is evident that the PC1-associated SST anomalies exhibit a significant "+ − +" teleconnection pattern in the North Atlantic. This pattern may be associated with the tri-pole SST anomaly forcing in the North Atlantic [41], with a notable negative correlation area extending northward from the negative correlation region in the Norwegian Sea to the Kara Sea. Notably, the tropical Atlantic region shows a positive correlation, suggesting that positive SST anomalies in this region may induce anomalous cyclonic circulation and upper-level divergence in its northwest due to the Gill effect [42]. This corresponds to the negative anomaly center in the mid-latitude region of the Atlantic (30–50° N), as depicted in Figure 4, resulting in the formation of a quasi-stationary Rossby wave train propagating northeastward and downstream.

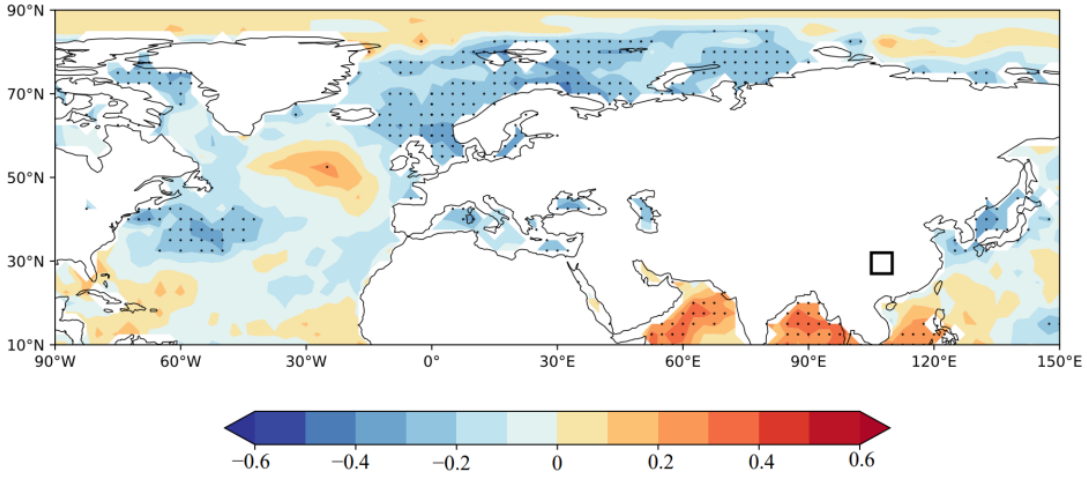

Figure 8. The correlation between the PC1 and simultaneous SST. The dotted regions in the figure indicate areas that pass the 90% reliability test.

It is worth noting that the Rossby wave train associated with PC1 exhibits negative anomalies in the upper troposphere, particularly in the Norwegian Sea and the Barents Sea regions, displaying pronounced intensified negative fluctuation amplitudes. Since

the lower layer in this region corresponds primarily to areas with notable interannual oscillations in sea ice coverage, the variability of sea ice anomalies in this region may have a certain modulation effect on the amplitude variation of the high-level Rossby wave train. To explore its possible cause, Figure 9 presents the correlation coefficients between PC1 and concurrent sea ice concentration over the past 60 years. It is evident that PC1 shows a significant positive correlation with sea ice concentration in the Barents Sea and Kara Sea. This significant correlation indicates that, when PC1 is positive, there is an abundance of sea ice in the vicinity of the Barents Sea and Kara Sea, leading to increased reflectivity in this region. Consequently, the solar shortwave radiation absorbed by the sea surface decreases, further strengthening the negative correlation between PC1 and SST in this area. Additionally, the excess sea ice near the Barents Sea induces local atmospheric cooling, which suppresses convective activity and further enhances the anomalous cyclonic circulation in the troposphere [32], thereby increasing the amplitude of the anomalous cyclonic circulation system in the Norwegian Sea and the Barents Sea regions.

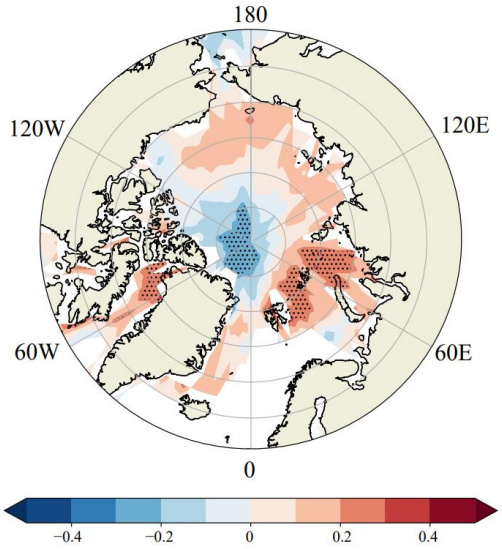

Figure 9. The correlation between the PC1 and simultaneous sea ice cover. The dotted regions in the figure indicate areas that pass a 90% confidence level *t*-test.

Based on the above analysis, we can summarize the conceptual diagram of the possible causes of summertime precipitation anomalies in the ESWC, as depicted in Figure 10. Anomalies in tropical SST in the North Atlantic induce cyclonic circulation in the mid-latitude region through the Gill effect. This, in turn, triggers the formation of a northeastward-propagating Rossby wave train, coupled with the "tri-pole" SST anomalies in the Atlantic. Additionally, the lower sea surface temperature near the Barents Sea leads to an abundance of sea ice and cooling of the air column, promoting the development of the wave train. The energy of the wave train disperses downstream and propagates to eastern China, resulting in cyclonic (anticyclonic) anomalies to the north (south) of the ESWC. These anomalies cause the convergence of low-latitude water vapor and high-latitude cold air, favoring regional precipitation formation in the ESWC. Consequently, this leads to above-normal summer precipitation in the ESWC, and vice versa.

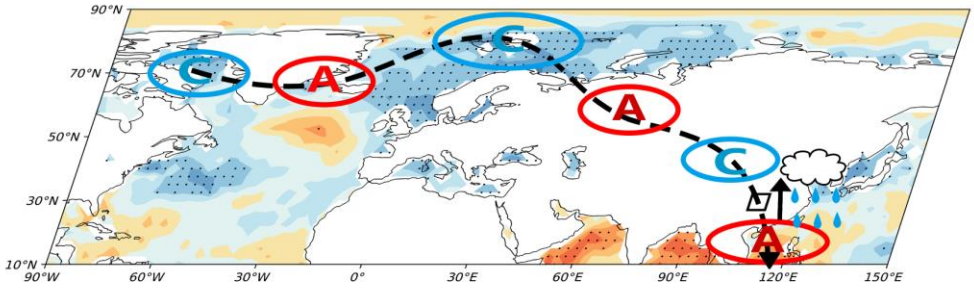

Figure 10. A conceptual diagram of the possible cause of summertime precipitation anomalies in the ESWC. The dotted line represents the propagation path of the wave activity flux.

4. Conclusions and Discussion

This paper combines station observations and reanalysis data to perform an empirical orthogonal function (EOF) analysis of summer precipitation in the ESWC over the past 60 years. This study investigates the spatial distribution and interannual variability characteristics of summer precipitation and further reveals possible physical mechanisms influencing the interannual variations of summer precipitation in the ESWC. The conclusions are as follows:

(1) At the interannual scale, the first two modes of summer precipitation in the ESWC are identified as the uniform pattern and the north–south dipole pattern, respectively. Among them, the uniform pattern dominates the variability of regional summer precipitation over the past 60 years, contributing to 52.9% of the total variance.

(2) When the uniform pattern (PC1) of summer precipitation in the ESWC strengthens, it is usually associated with cyclonic anomalies to the north of the ESWC and anticyclonic anomalies to the south of the ESWC. This meridional dipole pattern facilitates the convergence of high-latitude dry and cold air with the warm and moist southwesterly flow from the tropical ocean, promoting increased summer precipitation in the ESWC.

(3) The PC1 associated with tri-pole SST anomalies in the North Atlantic and sea ice anomalies near the Barents Sea significantly corresponds to a quasi-zonal wave train in the upper troposphere. This wave train propagates through the northwest Atlantic Ocean via the Norwegian Sea and western Europe, eventually reaching the ESWC. It induces the aforementioned "-+" circulation anomaly pattern near the ESWC, leading to increased regional summer precipitation.

An analysis of the possible causes of interannual variability in summer precipitation in the ESWC was conducted, along with an explanation of the corresponding physical mechanisms. However, future work should focus on further verification using numerical models. The variation of summertime precipitation in the ESWC is influenced by multiple driving factors, and this paper primarily considered the impact of SST in the northwestern Atlantic and sea ice in the vicinity of the Norwegian Sea and the Barents Sea on summer precipitation in the ESWC. In future research, other factors, such as the dynamic and thermal effects of the plateau, should also be taken into account. For the dynamic effect, an anomalous cyclonic structure that is constantly moving out will intensify convergence motion. In terms of the thermodynamic effect, the heating effect of the plateau will increase the instability of the air and strengthen the convective motion [43].

Author Contributions: Conceptualization, C.L. and D.H.; methodology, C.L.; writing—original draft preparation, D.H.; writing—review and editing, C.L., B.C. and Y.B. All authors have read and agreed to the published version of the manuscript.

Funding: This work was supported by the National Natural Science Foundation of China (41875111, 40975058, 42005120) and the 2020 Shanghai Science and Technology Innovation Action Plan: Social Development Science and Technology Research Project (20dz1200703).

Institutional Review Board Statement: Not applicable.

Informed Consent Statement: Not applicable.

Data Availability Statement: Not applicable.

Conflicts of Interest: The authors declare no conflict of interest.

References

1. Su, B.D.; Jiang, T.; Jin, W.B. Recent trends in observed temperature and precipitation extremes in the Yangtze River basin, China. *Theor. Appl. Climatol.* **2006**, *83*, 139–151. [CrossRef]
2. Pan, X.; Yin, Y.; Wang, X. Spatio-temporal characteristics and future trend of extreme precipitation in the Yangtze River Basin during 1960 to 2010. *Resour. Environ. Yangtze Basin* **2017**, *26*, 436–444. (In Chinese)
3. Ma, X.; Lin, A.; Fang, J. Research on spatio-temporal variation of extreme precipitation and extreme run off in the middle and lower reaches of Yangtze River from 1960–2010. *Geomat. Spat. Inf. Technol.* **2018**, *41*, 157–160+163. (In Chinese)
4. Bai, L.; Rong, Y. Reanalysis of the Characteristics of Extreme Rainfall in the Yangtze River Basin during Recent 50 Years. *J. Water Resour. Res.* **2015**, *4*, 88–100. (In Chinese) [CrossRef]
5. Li, Y.; Qing, J.; Li, Q.; Xiang, B. Features of western Pacific subtropical high (WPSH) associated with drought/flood in summer over the eastern part of Southwest China. *J. Southwest Univ.* **2013**, *3*, 11. (In Chinese)
6. Li, Y.; Zhou, J.; He, J.; Lu, C.; Xiang, B. Characteristics of Water Vapor Transport Associated with Abnormal Precipitation over the East of Southwestern China in June and July 2020. *Chin. J. Atmos. Sci.* **2022**, *46*, 309–326. (In Chinese)
7. Garcia-Herrera, R.A.; Paredes, D.; Trigo, R.M.; Trigo, I.F.; Hernández, E.; Barriopedro, D.; Mendes, M. The outstanding 2004/05 drought in the Iberian Peninsula: Associated atmospheric circulation. *J. Hydrometeorol.* **2007**, *8*, 483–498. [CrossRef]
8. Zhang, F.; Chen, T.; Zhang, F.; Shen, X.; Lan, Y. Extreme features of severe precipitation in meiyu period over the middle and lower reaches of Yangtze River Basin in June–July 2020. *Meteorol. Mon.* **2020**, *46*, 1405–1414. (In Chinese) [CrossRef]
9. Zhou, H.; Tang, H.; Cheng, B. The relation between East Asian summer monsoon and summer precipitation in Chongqing. *J. Southwest Univ.* **2010**, *32*, 81–88. (In Chinese)
10. Ma, Z.; Gao, W.; Liu, F.; Liu, Q. A study on monsoon circulations of drought and wet years on the east side of Qinghai-Xizang Plateau in early summer. *Plateau Meteorol.* **2003**, *S1*, 1–7. (In Chinese)
11. Ding, Y.; Sun, Y.; Liu, Y.; Si, D.; Wang, Z.; Zhu, Y.; Liu, Y.; Song, Y.; Zhang, J. Interdecadal and Interannual Variabilities of the Asian Summer Monsoon and Its Projection of Future Change. *Chin. J. Atmos. Sci.* **2013**, *37*, 253–280. (In Chinese)
12. Wang, Y.; Xiao, T.; Dong, X.; Li, Y.; Zhao, P. Influence of East Asian monsoon and South Asian monsoon synergy on summer precipitation in Southwest China. *Acta Meteorol. Sin.* **2021**, *79*, 541–557. (In Chinese)
13. Liang, L.; Li, Y.; Hu, H.; Jiang, X.; Zhang, E. Numerical study of influence of sensible heat anomalies in summer over Qinghai-Xizang Plateau on rainfall in Sichuan-Chongqing regions. *Plateau Meteorol.* **2013**, *32*, 1538–1545. (In Chinese) [CrossRef]
14. Ceng, S.; Gong, Y.; Lai, X. Impact of heat source over Qinghai-Xizang Plateau and its surrounding areas on rainfall in Sichuan-Chongqing Basin in summer. *Plateau Meteorol.* **2014**, *33*, 1182–1189. (In Chinese) [CrossRef]
15. Zhang, J.; Dong, W.; Fu, C.; Wu, L. The influence of vegetation cover on summer precipitation in China: A statistical analysis of NDVI and climate data. *Adv. Atmos. Sci.* **2003**, *20*, 1002–1006.
16. Hua, W.; Fan, G.; Zhou, D.; Li, H.; Liu, Y.; Li, X. Characteristics of winter and spring vegetation variation over Tibetan plateau and its influence on summer precipitation of southwest China. *Sci. Meteorol. Sin.* **2008**, *4*, 363–369. (In Chinese)
17. Hu, H. Relationship between snow anomaly in east of Qinghai-Tibet plateau and spring rainfall in Southwest China. *J. Arid Meteorol.* **2016**, *34*, 423–430. (In Chinese)
18. Li, Y.; Xiang, B.; Lu, C.; Ju, J.; Wang, N. Impact of Madden-Julian Oscillation activities on precipitation in summer over the east of Southwest China and its possible mechanism. *Chin. J. Atmos. Sci.* **2016**, *40*, 437–450. (In Chinese)
19. Chen, L. The effects of the anomalous sea-surface temperature of the equatorial Eastern Pacific Ocean on the tropical circulation and rainfall during the rainy period in China. *Chin. J. Atmos. Sci.* **1977**, *1*, 1–12. (In Chinese)
20. Tao, S.; Zhang, Q. Response of the Asian winter and summer monsoon to ENSO events. *Chin. J. Atmos. Sci.* **1998**, *22*, 399–407. (In Chinese)
21. Li, C.; Mu, M. The dipole in the equatorial Indian Ocean and its impacts on climate. *Chin. J. Atmos. Sci.* **2001**, *25*, 433–443. (In Chinese)
22. Li, Y.; Lu, C.; Xu, H.; Cheng, B. Anomalies of sea surface temperature in Pacafic-Indian Ocean and effects on drought/flood in summer over eastern of Southwest China. *J. Trop. Meteorol.* **2012**, *28*, 145–156. (In Chinese)
23. Lu, C.; Huang, L.; He, J.; Qin, Y. Interannual variability of heat content in Western Pacific warm pool and its impact on the Eastern Asian climatic anomaly. *J. Trop. Meteorol.* **2014**, *30*, 64–72. (In Chinese)
24. Chen, D.; Gao, S.; Chen, M.; Gao, S. The synergistic effect of SSTA between the equatorial eastern Pacific and the Indian-South China Sea warm pool region influence on the western Pacific subtropical high. *Haiyang Xuebao* **2016**, *38*, 1–15. (In Chinese)
25. Tang, H.; Wu, Y.; Dong, X.; Liu, X.; Wei, L.; Zhang, C. Impact analysis of equatorial Indian Ocean dipole on summer precipitation in Chongqing. *J. Mar. Meteorol.* **2020**, *40*, 52–61. (In Chinese)
26. Pang, Y.; Qin, N.; Wang, C.; Luo, Y. Analysis on the impact of ENSO events seasonal evolution on summer rainfall anomalies in Southwest China. *Plateau Meteorol.* **2020**, *39*, 581–593. (In Chinese) [CrossRef]

27. Li, Y.; Xu, H.; Gao, Y.; Li, Q. The characteristics of moisture transport associated with drought/flood in summer over the east of the southwestern China. *Acta Meteorol. Sin.* **2010**, *6*, 932–943. (In Chinese) [CrossRef]
28. Hersbach, H.; Bell, B.; Berrisford, P.; Hirahara, S.; Horányi, A.; Muñoz-Sabater, J.; Nicolas, J.; Peubey, C.; Radu, R.; Schepers, D.; et al. The ERA5 global reanalysis. *Q. J. R. Meteorol. Soc.* **2020**, *146*, 1999–2049. [CrossRef]
29. Takaya, K.; Nakamura, H. A Formulation of a Phase-Independent Wave-Activity Flux for Stationary and Migratory Quasi-geostrophic Eddies on a Zonally Varying Basic Flow. *J. Atmos. Sci.* **2001**, *58*, 608–627. [CrossRef]
30. Han, T.; He, S.; Wang, H.; Hao, X. Variation in Principal Modes of Midsummer Precipitation over Northeast China and Its Associated Atmospheric Circulation. *Adv. Atmos. Sci.* **2018**, *36*, 55–64. [CrossRef]
31. Yan, H.; Pan, X.; Zhu, Z.; Lu, R.; Li, L.; Tan, H. The two leading modes of winter clear-sky days over China and their formation mechanisms. *Clim. Dyn.* **2020**, *56*, 189–205. [CrossRef]
32. Lu, R.; Zhu, Z.; Li, T.; Pan, X.; Jiang, Y.; Lu, Y. Objective clustering of spatial patterns of summer extreme precipitation frequency over the Huaihe River Basin and their formation mechanisms. *Chin. J. Atmos. Sci.* **2021**, *45*, 1415–1432. (In Chinese)
33. Zhao, Y.; Park, C.; Son, S. Importance of Diabatic Heating for the Eastward-Moving Heavy Rainfall Events along the Yangtze River, China. *J. Atmos. Sci.* **2022**, *80*, 151–165. [CrossRef]
34. Wallace, J.M.; Gutzler, D.S. Teleconnections in the geopotential height field during the Northern Hemisphere winter. *Mon. Weather Rev.* **1981**, *109*, 784–812. [CrossRef]
35. Jin, D.; Guan, Z. Summer Rainfall Seesaw between Hetao and the Middle and Lower Reaches of the Yangtze River and Its Relationship with the North Atlantic Oscillation. *J. Clim.* **2017**, *30*, 6629–6643. [CrossRef]
36. Sardeshmukh, P.D.; Hoskins, B.J. The generation of global rotational flow by steady idealized tropical divergence. *J. Atmos. Sci.* **1988**, *45*, 1228–1251. [CrossRef]
37. Lu, C.; Ye, J.; Wang, S.; Yang, M.; Li, Q.; He, W.; Qin, Y.; Cai, J.; Mao, J. An Unusual Heat Wave in North China During Midsummer, 2018. *Front. Earth Sci.* **2020**, *8*, 238. [CrossRef]
38. Peng, S.; Whitaker, J.S. Mechanisms determining the atmospheric response to midlatitude SST anomalies. *J. Clim.* **1999**, *12*, 1393–1408. [CrossRef]
39. Peng, S.; Robinson, W.A.; Li, S. Mechanisms for the NAO responses to the North Atlantic SST tripole. *J. Clim.* **2003**, *16*, 1987–2004. [CrossRef]
40. Wu, R.; Yang, S.; Liu, S.; Sun, L.; Lian, Y.; Gao, Z. Northeast China summer temperature and North Atlantic SST. *J. Geophys. Res.* **2011**, *116*, D16. [CrossRef]
41. Zuo, J.; Li, W.; Sun, C.; Xu, L.; Ren, H. Impact of the North Atlantic sea surface temperature tripole on the East Asian summer monsoon. *Adv. Atmos. Sci.* **2013**, *30*, 1173–1186. [CrossRef]
42. Gill, A.E. Some simple solutions for heat-induced tropical circulation. *Q. J. R. Meteorol. Soc.* **1980**, *106*, 447–462. [CrossRef]
43. Zhao, Y.; Chen, D.; Deng, Y.; Son, S.; Wang, X.; Di, D.; Pan, M.; Ma, X. How Were the Eastward-Moving Heavy Rainfall Events from the Tibetan Plateau to the Lower Reaches of the Yangtze River Enhanced? *J. Clim.* **2020**, *34*, 607–620. [CrossRef]